Numerical Modeling of Fluid-Saturated Porous Sample Loading Based on Thermodynamically Compatible System Theory

Mikhail Novikov[1,2(✉)], Vadim Lisitsa[1], and Evgeniy Romenski[2]

[1] Trofimuk Institute of Petroleum Geology and Geophysics SB RAS, Novosibirsk 630090, Russia
novikovma@ipgg.sbras.ru
[2] Sobolev Institute of Mathematics SB RAS, Novosibirsk 630090, Russia
evrom@math.nsc.ru

Abstract. A quasi-static approximation of a thermodynamically compatible system of PDEs is presented to model the loading test for a two-phase (solid-fluid) sample. To numerically solve the resulting PDEs written in terms of displacements, we use a second-order finite-difference scheme on a staggered grid. Numerical results demonstrate the application of the presented approach to estimate seismic attenuation in two-phase media on different scales, involving an effective porosity model of fractured media on the mesoscale or the geometry of a single pore directly at the microscale.

Keywords: Numerical rock physics · Thermodynamically compatible systems · Poroelasticity · Quasistatic modeling · Finite differences

1 Introduction

The last decades of studying the non-elastic behavior of fluid-saturated rocks demonstrated that seismic attributes allow for the identification of the internal structure of heterogeneous formations and fluid mobility within them. These studies have potential applications in fractured reservoir monitoring for different purposes: oil recovery enhancement, carbon dioxide sequestration, and thermal energy production. As the fractured rock usually has a multiscale structure, several phenomena causing nonelastic behavior occur. In particular, in the presence of fluid within a heterogeneous porous rock, fluid flows occur both between heterogeneities (for example, fractures) and between pores. The first type mentioned is called wave-induced fluid flow (WIFF), which affects the velocity and attenuation of propagating seismic waves widely in the seismoacoustic frequency range [1]. WIFF intensity depends on the physical properties contrast between host

This work was supported by the Russian Science Foundation grant no. 19-77-20004.

© The Author(s), under exclusive license to Springer Nature Switzerland AG 2024
O. Gervasi et al. (Eds.): ICCSA 2024 Workshops, LNCS 14817, pp. 237–249, 2024.
https://doi.org/10.1007/978-3-031-65238-7_16

rock and heterogeneities and also their connectivity in the considered domain. Second, microscale phenomena is called squirt-flow [2]. It depends mostly on the fluid properties and explicit geometry of a single pore in the medium. Thus, modeling mesoscale fluid flows such as WIFF requires a fairly large computational domain (compared to the pore size) in terms of representativeness of the heterogeneous structure, and a two-phase medium (solid + liquid) can only be effectively described if both phases are present at every point on the continuum. In contrast, considering a single pore when modeling its geometry can only be done with explicit phase division. As a result, it is impossible to properly take into account fluid flow processes on different scales in one modeling cycle, and if the effective mathematical model of two-phase media has some limitations on one phase transition, one cannot apply only one model to investigate fluid flow at all scales. While the first problem is usually caused by overwhelming computational costs, the second one seems more solvable by introducing the universal model to describe two-phase media, including single-phase limits.

One of the actively developing approaches nowadays is based on the theory of Symmetric Hyperbolic Thermodynamically Compatible (SHTC) systems of conservation laws [3,4]. This theory is a powerful tool for developing new mathematically well-posed models whose governing equations satisfy the laws of irreversible thermodynamics. Our studies are based on SHTC models of porous media, considered as a two-phase mixture of solid and liquid, presented in [5–8]. One of the main advantages of the SHTC porous media model is that it describes the behavior of the medium for the entire porosity range from 0 to 1. It also allows the diffuse interface approach to be used for modeling in regions with interfaces between media with different porosities, including pure fluid and pure elastic media.

The rest of the paper is organized as follows. Section 2 briefly describes the linear SHTC governing equations for wave propagation in a saturated porous medium and their transformed form, which is then used to model quasistatic loading. In Sect. 3, we present a finite-difference approximation of the quasi-static equations and approximate the boundary conditions that close the resulting system of equations. In Sect. 4, we consider numerical modeling of the uniaxial loading of a synthetic fractured rock sample to validate the presented method. The results of these experiments are demonstrated and described in Sect. 5. Finally, in the conclusion, we summarize the presented algorithm and discuss its possible applications.

2 Quasi-Static Approximation for Poroelastic Model

In our work, we consider a 2D system of equations governing small-amplitude wave propagation in an elastic porous fluid-saturated medium:

$$\begin{gathered}
\rho \frac{\partial v^i}{\partial t} + \frac{\partial p}{\partial x_i} - \frac{\partial s_{ik}}{\partial x_k} = 0, \\
\frac{\partial q^k}{\partial t} + \left(\frac{1}{\rho_1} - \frac{1}{\rho_2} \right) \frac{\partial p}{\partial x_k} = -\frac{c_1 c_2}{\theta} q^k, \\
\frac{\partial p}{\partial t} + K \frac{\partial v^k}{\partial x_k} + \frac{\alpha_1 \alpha_2}{\rho} \left(\rho_2 - \rho_1 \right) K \frac{\partial q^k}{\partial x_k} = 0, \\
\frac{\partial s_{ik}}{\partial t} - \mu \left(\frac{\partial v^i}{\partial x_k} + \frac{\partial v^k}{\partial x_i} - \frac{2}{3} \delta_{ik} \frac{\partial v^j}{\partial x_j} \right) = -\frac{s_{ik}}{\tau}.
\end{gathered} \tag{1}$$

Here, we use Einstein notation to represent summation. The system (1) describes two vector fields of fluid-solid mixture velocity $\vec{v} = (v^1\ v^2)^T$ and relative fluid velocity $\vec{q} = (q^1\ q^2)^T$, scalar field of fluid pressure p and a tensor field of deviatoric stress

$$\boldsymbol{s} = \begin{pmatrix} s_{11} & s_{12} \\ s_{12} & s_{22} \end{pmatrix}. \tag{2}$$

Note that it is convenient here to consider the deviatoric part of the stress tensor, and to recover the full stress tensor $\boldsymbol{\sigma}$ one should combine $\boldsymbol{s}$ with fluid pressure [5]. The coefficients of Eqs. (1) include the material properties of both phases. We refer lower indices for material constants 1 and 2 corresponding to fluid and solid phases, consequently. Here α_1 and α_2 are volume fractions of fluid and solid phases (α_1 is porosity and $\alpha_2 = 1 - \alpha_1$); ρ, ρ_1 and ρ_2 are mixture, fluid and solid densities; $c_i = \alpha_i \rho_i / \rho$ ($i \in 1, 2$) are mass fractions of the phases. The effective elastic properties of a mixture are defined by the bulk modulus K and shear modulus μ. Note that as we consider a two-phase mixture of solid and inviscid fluid, these moduli are connected with single-phase moduli as follows:

$$K = \left(\frac{\alpha_1}{K_1} + \frac{\alpha_2}{K_2} \right)^{-1}, \quad \mu = \alpha_2 \mu_2. \tag{3}$$

Finally, θ and τ represent the interfacial friction coefficient and relaxation time [8]. In our work, we consider the limit case $\tau \to \infty$, so the right-side term of the fourth equation in (1) vanishes.

A popular approach to investigate the fluid flow within a heterogeneous poroelastic medium is a quasi-static modeling, as it allows one to consider the representative volume of the medium under loading at a wide range of frequencies without any domain expansion due to satisfy the typical scale of the process, defined by the wavelength. To observe fluid motion distribution, it is convenient to apply the quasi-static approximation because dynamic modeling results in high wave scattering at high frequencies [9]. We convert the system (1) into a quasi-static formulation with mixture displacement $\vec{u} = (u^1\ u^2)^T$ and relative fluid displacement $\vec{w} = (w^1\ w^2)^T$. To do so, we neglect the acceleration terms and reformulate the system in displacement-stress form. As a result, we obtain the system

$$\begin{gathered} \frac{\partial p}{\partial x_i} - \frac{\partial \sigma_{ik}}{\partial x_k} = 0, \\ \left(\frac{1}{\rho_1} - \frac{1}{\rho_2} \right) \frac{\partial p}{\partial x_k} = -\frac{c_1 c_2}{\theta} \frac{\partial w^k}{\partial t}, \\ \frac{\partial p}{\partial t} + K \frac{\partial^2 u^k}{\partial t \partial x_k} + \frac{\alpha_1 \alpha_2}{\rho} (\rho_2 - \rho_1) K \frac{\partial^2 w^k}{\partial t \partial x_k} = 0, \\ \frac{\partial s_{ik}}{\partial t} - \mu \left(\frac{\partial^2 u^i}{\partial t \partial x_k} + \frac{\partial u^k}{\partial t \partial x_i} - \frac{2}{3} \delta_{ik} \frac{\partial^2 u^j}{\partial t \partial x_j} \right) = 0. \end{gathered} \tag{4}$$

After this, we perform the Fourier transform to neglect the time derivatives and obtain

$$\begin{gathered}\frac{\partial p}{\partial x_i}-\frac{\partial s_{ik}}{\partial x_k}=0,\\ \left(\frac{1}{\rho_1}-\frac{1}{\rho_2}\right)\frac{\partial p}{\partial x_k}=-i\frac{c_1c_2}{\theta}\omega w^k,\\ p+K\frac{\partial u^k}{\partial x_k}+\frac{\alpha_1\alpha_2}{\rho}\left(\rho_2-\rho_1\right)K\frac{\partial w^k}{\partial x_k}=0,\\ s_{ik}-\mu\left(\frac{\partial u^i}{\partial x_k}+\frac{\partial u^k}{\partial x_i}-\frac{2}{3}\delta_{ik}\frac{\partial u^j}{\partial x_j}\right)=0,\end{gathered}\tag{5}$$

where ω is the frequency. Substituting the fluid pressure and stress component expressions from the third and fourth equations into the first and second equations in (5), we can obtain a closed second-order PDE system on displacements:

$$\begin{gathered}\frac{\partial}{\partial x_i}\left[K\frac{\partial u^k}{\partial x_k}+N\frac{\partial w^k}{\partial x_k}\right]+\frac{\partial}{\partial x_k}\left[\mu\left(\frac{\partial u^i}{\partial x_k}+\frac{\partial u^k}{\partial x_i}-\frac{2}{3}\delta_{ik}\frac{\partial u^j}{\partial x_j}\right)\right]=0,\\ \frac{\partial}{\partial x_j}\left[K\frac{\partial u^k}{\partial x_k}+N\frac{\partial w^k}{\partial x_k}\right]=iL\omega w^j.\end{gathered}\tag{6}$$

In component-wise form, this system reads as

$$\begin{gathered}\frac{\partial}{\partial x_1}\left[\left(K+\frac{4}{3}\mu\right)\frac{\partial u^1}{\partial x_1}+\left(K-\frac{2}{3}\mu\right)\frac{\partial u^2}{\partial x_2}+N\left(\frac{\partial w^1}{\partial x_1}+\frac{\partial w^2}{\partial x_2}\right)\right]\\ +\frac{\partial}{\partial x_2}\left[\mu\left(\frac{\partial u^1}{\partial x_2}+\frac{\partial u^2}{\partial x_1}\right)\right]=0,\\ \frac{\partial}{\partial x_2}\left[\left(K-\frac{2}{3}\mu\right)\frac{\partial u^1}{\partial x_1}+\left(K+\frac{4}{3}\mu\right)\frac{\partial u^2}{\partial x_2}+N\left(\frac{\partial w^1}{\partial x_1}+\frac{\partial w^2}{\partial x_2}\right)\right]\\ +\frac{\partial}{\partial x_1}\left[\mu\left(\frac{\partial u^1}{\partial x_2}+\frac{\partial u^2}{\partial x_1}\right)\right]=0,\\ \frac{\partial}{\partial x_1}\left[K\left(\frac{\partial u^1}{\partial x_1}+\frac{\partial u^2}{\partial x_2}\right)+N\left(\frac{\partial w^1}{\partial x_1}+\frac{\partial w^2}{\partial x_2}\right)\right]=iL\omega w^1,\\ \frac{\partial}{\partial x_2}\left[K\left(\frac{\partial u^1}{\partial x_1}+\frac{\partial u^2}{\partial x_2}\right)+N\left(\frac{\partial w^1}{\partial x_1}+\frac{\partial w^2}{\partial x_2}\right)\right]=iL\omega w^2.\end{gathered}\tag{7}$$

For simplicity, here we denote

$$\begin{gathered}N=\frac{\alpha_1\alpha_2}{\rho}K(\rho_2-\rho_1),\\ L=\frac{c_1c_2}{\theta}\left(\frac{1}{\rho_1}-\frac{1}{\rho_2}\right)^{-1}.\end{gathered}\tag{8}$$

System (7) allows us to obtain displacements first and then recover pressure and stress components using the last two equations from (5). To set a boundary value problem in a limited domain Ω with boundary $\partial\Omega$ boundary conditions should be defined. In our case, we define the normal stress and restrict the fluid displacement at the boundary:

$$\begin{gathered}\boldsymbol{\sigma}\cdot\vec{n}|_{\partial\Omega}=\vec{\phi}(\vec{x}),\\ \mathbf{w}\cdot\vec{n}|_{\partial\Omega}=0.\end{gathered}\tag{9}$$

Here $\vec{n}$ is the external normal vector to the boundary, and $\vec{\phi}(\vec{x})$ is a smooth enough function defined at the boundary ($\vec{x}\in\partial\Omega$). In particular, further we will be considering the rectangular domain $\Omega=\{\vec{x}:x_1\in[x_{10},x_{11}],\ x_2\in[x_{20},x_{21}]\}$ (Fig. 1, left). In this case, the boundary $\partial\Omega$ consists of straight line segments

aligned parallel to axes. For example, for the left and right sides of the rectangle boundary $\partial\Omega_L = \{x : x_1 \in [x_{10}, x_{11}],\ x_2 = x_{11}\}$ and $\partial\Omega_R = \{x : x_1 \in [x_{10}, x_{11}],\ x_2 = x_{21}\}$ the component-wise form of the boundary conditions with the use of third and fourth equations of (5) gives

$$\begin{gathered} \sigma_{11} = \left(K + \tfrac{4}{3}\mu\right)\frac{\partial u^1}{\partial x_1} + \left(K - \tfrac{2}{3}\mu\right)\frac{\partial u^2}{\partial x_2} + N\left(\frac{\partial w^1}{\partial x_1} + \frac{\partial w^2}{\partial x_2}\right) = \phi_{11}, \\ \sigma_{13} = \mu\left(\frac{\partial u^1}{\partial x_2} + \frac{\partial u^2}{\partial x_1}\right) = \phi_{13}, \\ w_1 = 0. \end{gathered} \tag{10}$$

Similarly, for the rest of the boundary, we assume boundary conditions on σ_{33}, σ_{13}, and ω_3:

$$\begin{gathered} \sigma_{33} = \left(K - \tfrac{4}{3}\mu\right)\frac{\partial u^1}{\partial x_1} + \left(K + \tfrac{2}{3}\mu\right)\frac{\partial u^2}{\partial x_2} + N\left(\frac{\partial w^1}{\partial x_1} + \frac{\partial w^2}{\partial x_2}\right) = \phi_{33}, \\ \sigma_{13} = \mu\left(\frac{\partial u^1}{\partial x_2} + \frac{\partial u^2}{\partial x_1}\right) = \phi_{13}, \\ w_3 = 0. \end{gathered} \tag{11}$$

3 Numerical Method

Numerical solution of Eqs. (7) within a rectangular domain $\Omega = [x_{10}, x_{11}] \times [x_{20}, x_{21}]$ implies finite differences approximating the derivatives on a staggered grid (Fig. 1), resulting in a second-order finite-difference scheme. The computational domain is presented by a regular rectangular grid with grid steps Δx_1 and Δx_2 in axes directions. The grid contains nodes where different variables are defined and different equations are stated. From now on, $i,\ j \in \mathbb{Z}$. First node group with indices $(i, j + 1/2)$ $(i = \overline{1, N_1 - 1},\ j = \overline{0, N_2 - 1})$, or with node coordinates $\vec{x} = ((i - 1/2)\Delta x_1, j\Delta x_2)$, store displacement components u^1, w^1 and second derivatives of these components. Second components of displacement vectors u^2, w^2 with their second derivatives are defined at node group with indices $(i + 1/2, j)$ and coordinates $(i\Delta x_1, (j - 1)\Delta x_2)$ $(i = \overline{0, N_1 - 1},\ j = \overline{1, N_2 - 1})$. Finally, we define material properties by the constants presented above in nodes with indices $(i + 1/2, j + 1/2)$ and coordinates $(i\Delta x_1, j\Delta x_2)$ $(i = \overline{0, N_1 - 1},\ j = \overline{0, N_2 - 1})$. First derivatives are approximated by second-order central differences:

$$\begin{aligned}
&\frac{\left(K+\frac{4}{3}\mu\right)_{i+1/2,j+1/2}D_1[u^1]_{i+1/2,j+1/2}-\left(K+\frac{4}{3}\mu\right)_{i-1/2,j+1/2}D_1[u^1]_{i-1/2,j+1/2}}{\Delta x_1}\\
&+\frac{\left(K-\frac{2}{3}\mu\right)_{i+1/2,j+1/2}D_2[u^2]_{i+1/2,j+1/2}-\left(K-\frac{2}{3}\mu\right)_{i-1/2,j+1/2}D_2[u^2]_{i-1/2,j+1/2}}{\Delta x_1}\\
&+\frac{(N)_{i+1/2,j+1/2}D_1[w^1]_{i+1/2,j+1/2}-(N)_{i-1/2,j+1/2}D_1[w^1]_{i-1/2,j+1/2}}{\Delta x_1}\\
&+\frac{(N)_{i+1/2,j+1/2}D_2[w^2]_{i+1/2,j+1/2}-(N)_{i-1/2,j+1/2}D_2[w^2]_{i-1/2,j+1/2}}{\Delta x_1}\\
&+\frac{(\mu)_{i,j+1}D_2[u^1]_{i,j+1}-(\mu)_{i,j}D_2[u^1]_{i,j}}{\Delta x_2}+\frac{(\mu)_{i,j+1}D_1[u^2]_{i,j+1}-(\mu)_{i,j}D_1[u^2]_{i,j}}{\Delta x_2}=0,
\end{aligned}$$

$$\begin{aligned}
&\frac{\left(K-\frac{2}{3}\mu\right)_{i+1/2,j+1/2}D_1[u^1]_{i+1/2,j+1/2}-\left(K-\frac{2}{3}\mu\right)_{i+1/2,j-1/2}D_1[u^1]_{i+1/2,j-1/2}}{\Delta x_2}\\
&+\frac{\left(K+\frac{4}{3}\mu\right)_{i+1/2,j+1/2}D_2[u^2]_{i+1/2,j+1/2}-\left(K+\frac{4}{3}\mu\right)_{i+1/2,j-1/2}D_2[u^2]_{i+1/2,j-1/2}}{\Delta x_2}\\
&+\frac{(N)_{i+1/2,j+1/2}D[w^1]_{i+1/2,j+1/2}-(N)_{i+1/2,j-1/2}D[w^1]_{i+1/2,j-1/2}}{\Delta x_2}\\
&+\frac{(N)_{i+1/2,j+1/2}D_2[w^2]_{i+1/2,j+1/2}-(N)_{i+1/2,j-1/2}D_2[w^2]_{i+1/2,j-1/2}}{\Delta x_2}\\
&+\frac{(\mu)_{i+1,j}D_2[u^1]_{i+1,j}-(\mu)_{i,j}D_2[u^1]_{i,j}}{\Delta x_1}+\frac{(\mu)_{i+1,j}D_1[u^2]_{i+1,j}-(\mu)_{i,j}D_1[u^2]_{i,j}}{\Delta x_1}=0,
\end{aligned}\tag{12}$$

$$\begin{aligned}
&\frac{(K)_{i+1/2,j+1/2}D_1[u^1]_{i+1/2,j+1/2}-(K)_{i-1/2,j+1/2}D_1[u^1]_{i-1/2,j+1/2}}{\Delta x_1}\\
&+\frac{(K)_{i+1/2,j+1/2}D_2[u^2]_{i+1/2,j+1/2}-(K)_{i-1/2,j+1/2}D_2[u^2]_{i-1/2,j+1/2}}{\Delta x_1}\\
&\frac{(N)_{i+1/2,j+1/2}D_1[w^1]_{i+1/2,j+1/2}-(N)_{i-1/2,j+1/2}D_1[w^1]_{i-1/2,j+1/2}}{\Delta x_1}\\
&\frac{(N)_{i+1/2,j+1/2}D_2[u^2]_{i+1/2,j+1/2}-(N)_{i-1/2,j+1/2}D_2[u^2]_{i-1/2,j+1/2}}{\Delta x_1}\\
&=i\omega\left(L\right)_{i,j+1/2}\left(w^1\right)_{i,j+1/2},
\end{aligned}$$

$$\begin{aligned}
&\frac{(K)_{i+1/2,j+1/2}D_1[u^1]_{i+1/2,j+1/2}-(K)_{i+1/2,j-1/2}D_1[u^1]_{i+1/2,j-1/2}}{\Delta x_2}\\
&+\frac{(K)_{i+1/2,j+1/2}D_2[u^2]_{i+1/2,j+1/2}-(K)_{i+1/2,j-1/2}D_2[u^2]_{i+1/2,j-1/2}}{\Delta x_2}\\
&\frac{(N)_{i+1/2,j+1/2}D_1[w^1]_{i+1/2,j+1/2}-(N)_{i+1/2,j-1/2}D_1[w^1]_{i+1/2,j-1/2}}{\Delta x_2}\\
&\frac{(N)_{i+1/2,j+1/2}D_2[u^2]_{i+1/2,j+1/2}-(N)_{i+1/2,j-1/2}D_2[u^2]_{i+1/2,j-1/2}}{\Delta x_2}\\
&=i\omega\left(L\right)_{i+1/2,j}\left(w^2\right)_{i+1/2,j}.
\end{aligned}$$

$$D_1[f]_{I,J}=\frac{f_{I+1/2,J}-f_{I-1/2,J}}{\Delta x_1},\quad D_2[f]_{I,J}=\frac{f_{I,J+1/2}-f_{I,J-1/2}}{\Delta x_2}\tag{13}$$

I and J in differences (13) are either integer or non-integer, and $f\in\{u^1,u^2,w^1,w^2\}$. Second derivatives are approximated by using formulae (13) twice recursively. With the definition of discrete displacement fields and finite differences described above, we approximate the first and third equations of the system (7) at nodes with indices $(i,j+1/2)$ and the second and fourth equations

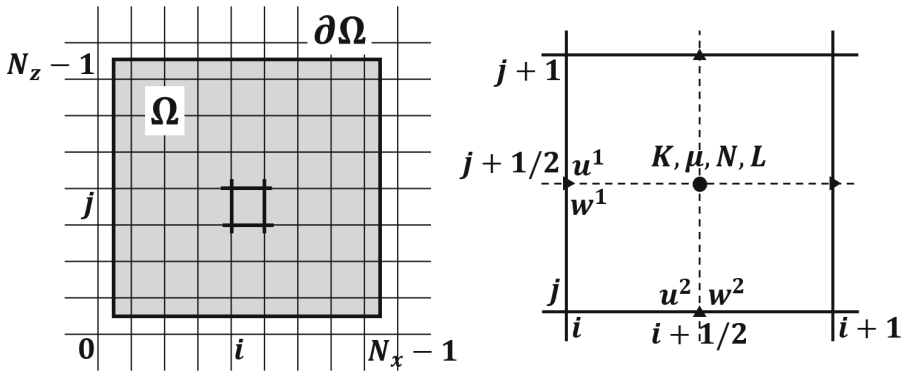

Fig. 1. Schematic images of the computational domain with grid (left) and grid cell (right).

in (7) at nodes with indices $(i+1/2, j)$. As a result, we approximate the system (7) with the following scheme:

However, not all coefficients are defined at the nodes where they appear in the scheme. In particular, in the first two equations of the system (12) shear module μ should be taken from nodes (i, j), where it is not defined explicitly, and an analogous situation happens with the coefficient L in the last pair of equations of (12). To keep the order of approximation in such cases, we apply the balance method [10] and, as a result, substitute average values using neighboring nodes of values defined as follows:

$$(\mu)_{i,j} = \frac{1}{4}\left[\frac{1}{(\mu)_{i-1/2,j-1/2}} + \frac{1}{(\mu)_{i-1/2,j+1/2}} + \frac{1}{(\mu)_{i+1/2,j-1/2}} + \frac{1}{(\mu)_{i+1/2,j+1/2}}\right]^{-1},$$
$$(L)_{i,j+1/2} = \frac{(L)_{i-1/2,j+1/2}+(L)_{i+1/2,j+1/2}}{2},$$
$$(L)_{i+1/2,j} = \frac{(L)_{i+1/2,j-1/2}+(L)_{i+1/2,j+1/2}}{2}. \tag{14}$$

As we assume the computational domain to be rectangular with the boundary going through the centers of the grid cells, in boundary nodes and near-boundary nodes, the presented Eqs. (12) make no sense because some variables appear at the nodes where they are not defined. To get rid of the undefined values and complete the resulting system in all the computational domain, we take into account boundary conditions at these nodes. In particular, we modify the Eqs. (12) using the immersed boundary technique [11] by the boundary values approximation. For example, at the left side of the boundary $\partial\Omega_L$ $(i = 1/2)$ we apply conditions (10) for the solution components and analogous grid function $(\sigma_{13})_{i,j}$ in the following way:

$$
\begin{gathered}
(\phi_{11})_{1/2,j+1/2} = (\sigma_{11})_{1/2,j+1/2} = \\
(K + \tfrac{4}{3})_{1/2,j+1/2} \frac{(u^1)_{1,j+1/2} - (u^1)_{0,j+1/2}}{\Delta x_1} + (K - \tfrac{2}{3})_{1/2,j+1/2} \frac{(u^2)_{1/2,j+1} - (u^2)_{1/2,j}}{\Delta x_2} \\
+ (N)_{1/2,j+1/2} \left(\frac{(w^1)_{1,j+1/2} - (w^1)_{1,j+1/2}}{\Delta x_1} + \frac{(w^2)_{1/2,j+1} - (w^2)_{1/2,j}}{\Delta x_2} \right), \\
(\sigma_{13})_{1,j} = \frac{(\sigma_{13})_{1/2,j} + (\sigma_{13})_{3/2,j}}{2} = \frac{(\phi_{13})_{1/2,j} + (\sigma_{13})_{3/2,j}}{2}. \\
\frac{(w^1)_{0,j+1/2} - (w^2)_{1,j+1/2}}{2} = 0,
\end{gathered}
\tag{15}
$$

The first and third equations of (15) are used to exclude $(u^1)_{0,j+1/2}$ and $(w^1)_{0,j+1/2}$ from the first and third equations of (12). The second equation of (15) according to the first equation of (5) is used to exclude $(u^1)_{0,j}$ and $(u^2)_{-1/2,j}$ from the last two terms in the second equation of (12). As a result, we obtain a closed system of linear equations to calculate displacements. Such systems can be solved by different approaches, including direct and iterative solvers. In our case, we apply Intel MKL PARDISO solver.

4 Numerical Experiment of Heterogeneous Sample Loading

To test the described algorithm, we perform numerical experiments of square sample loading in the x_1-axis direction. So we only apply non-zero normal stress σ_{11} at the boundary parts $\partial\Omega_L$ and $\partial\Omega_R$. Such numerical experiments were carried out, for example, to study wave-induced fluid flows within fractured fluid-saturated media [12–15] or estimate seismic attenuation caused by fluid flow as a part of the upscaling algorithm, where heterogeneous fluid-saturated media is approximated by an equivalent homogeneous viscoelastic media in terms of the same reaction to the same loading.

In a first test, the computational domain is presented by heterogeneous porous fluid-saturated medium (Fig. 2, left), where heterogeneities are fractures filled with more porous material, which provides more intensive fluid mobility due to the larger interfacial friction coefficient θ. The sizes of the domain in x_1 and x_2 directions are 1 m, and the single fracture is a rectangle of 0.004 m width and 0.03 m length. As can be seen in Fig. 2, single fractures form clusters going through the whole domain. The computational domain has 500 grid cells in both axes directions with a grid step of 0.002 m. Physical parameters of background and fracture-filling material models are presented in Table 1.

As we want to demonstrate the possibility of investigating wave-induced fluid flow appearing in the rock sample, we consider both low- and high-frequency cases in our experiments. We do so because fracture-to-background fluid flow usually develops intensively at relatively low frequencies, when the most intensive fracture-to-fracture fluid flow appears at relatively high ones [13,15]. To see the difference in fluid flow processes, we make two experiments of uniaxial loading at 10 Hz and 1 MHz.

The second test of sample uniaxial loading is aimed at studying the possibility of the approach to cover cases close to limit ones, where single-phase

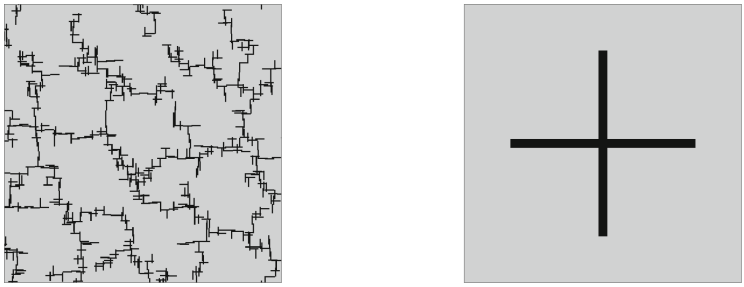

Fig. 2. Synthetic sample of fractured media (left): black color represents fractures, and gray color represents background. Model with fluid-filled cross subdomain (right): black color represents the material with porosity 0.999, gray color represents the material with porosity 0.001.

Table 1. Material properties for fractured media: background (second column) and fracture-filling material (third column); properties for media with cross: background (fourth column) and cross content (fifth column).

Parameter	Material 1	Material 2	Material 3	Material 4
Fluid density, ρ_1 $[kg/m^3]$	1040	1040	1040	1040
Solid density, ρ_2 $[kg/m^3]$	2500	2500	2500	2500
Interfacial friction coefficient, θ $[s]$	$3.36 \cdot 10^{-13}$	$3.36 \cdot 10^{-1}$	$7.8 \cdot 10^{-18}$	$4.48 \cdot 10^{-17}$
Mixture bulk modulus, K $[Pa]$	$3.94 \cdot 10^{10}$	$9.48 \cdot 10^{9}$	$3.94 \cdot 10^{10}$	$2.4 \cdot 10^{9}$
Solid shear modulus, μ $[Pa]$	$2.45 \cdot 10^{10}$	$2.45 \cdot 10^{10}$	$4.4 \cdot 10^{10}$	10^{6}
Porosity	0.05	0.2	0.001	0.999

materials (fluid, solid) are presented within the medium. Single-phase consideration is required to model fluid motion within pore space explicitly, including the pore geometry [16,17]. The problem set up is close to one in [2], where two models for fluid/solid two-phase media representation were compared. The computational domain here (Fig. 2, right) is presented by the almost purely solid background material (porosity $\alpha_1 = 0.001$), storing a cross-form subdomain containing almost only fluid (porosity $\alpha_1 = 0.999$). The square computational domain has 0.03 m sides, and the cross is formed by the intersection of two rectangular segments with a width of 0.001 m and a length of 0.02 m. Physical properties are presented in Table 1. We again apply loading along the x_1 axis, and the frequency is 1 GHz.

5 Numerical Results

In this section, we present the results of the numerical solution of Eqs. (7) using the approximation (12) for the two considered mediums (Fig. 2) described above.

In particular, we consider the corresponding part of the solution $\vec{w}$ and demonstrate its module $|\vec{w}|$ at Fig. 3 to investigate the fluid mobility within the heterogeneous media by showing the zones of intensive fluid flow and its behavior under loading at different frequencies.

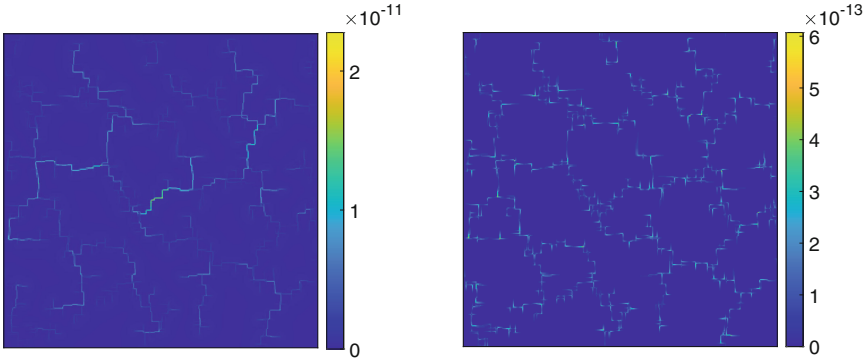

Fig. 3. Relative fluid displacement module $|\vec{w}|$ [m] within fractured media under uniaxial loading at 10 Hz (left) and 1 MHz (right).

For the first set up, fractured media in Fig. 3 we can clearly see that the most fluid motion is concentrated within the fractures, as expected, because the fluid mobility is significantly limited by the value of the interfacial friction coefficient. However, in the case of lower frequency (Fig. 3, left) we notice fluid displacement relatively small but comparable to one between the fractures. This motion represents exactly the FB-WIFF type, spreading in the fractures vicinity from the fractures. One can also observe the global nature of fluid displacement within the fracture clusters, considering it some kind of smoothed, meaning that the smallest parts of the structures (single fracture parts) are not affected by relative fluid displacement. It is caused by the characteristic length of the phenomena defined by the frequency (analogous to the wave propagation case, when the wavelength does not allow for oscillations to develop in significantly smaller structures in propagation time). Conversely, the high-frequency case results in no fluid displacement of order of one within the fractures, as demonstrated in Fig. 3. Here, we can only detect significant fluid displacement within the fractures. More specifically, this displacement consists of the smaller (in terms of the typical distance) perturbations that highlight the whole fracture system, including the smallest embranchments comparable to a single fracture size. So both frequency cases result in the observable fluid flow between the fractures (FF-WIFF), but the behavior of these flows in these two cases is obviously not the same. Note that even if we see the orders of displacement moduli in both cases, we cannot compare the intensities of fluid motion between the two cases yet, as for this the absolute (and not relative, as in the Fig. 3) values of displacements should be considered. Finally, all observed behavior is qualitatively similar to

an analogous study performed using Biot theory [13]. Unfortunately, we have no possibility to compare quantitatively results based on our mathematical model and Biot model due to the sufficiently different nature of their origins, and the same material properties for both models can result in different responses [5].

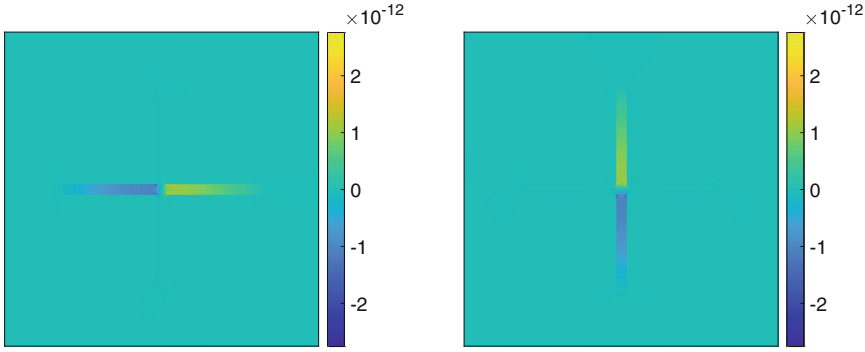

Fig. 4. Relative fluid displacement module components w_1 (left) and w_2 (right) [m]. in media with the fluid-saturated cross-form subdomain.

In the second case (media with cross-form heterogeneity), relative fluid displacement $\vec{w}$ can be interpreted as an absolute one, and the mixture displacement $\vec{u}$ should be ignored, because in the considered mathematical model (1) reducing the solid phase part in the mixture to zero (i.e. $\alpha_1 \to 1$) results in the mixture velocity losing its physical sense within the system of equations and acting independently on the described fluid model. In the assumption of holding this property also in the quasi-static approximation of the model, we consider only fluid motion in the cross subdomain. Fluid displacement component fields w_1 and w_2 are demonstrated in Fig. 4. We observe the predictable symmetric behavior of fluid motion, with its intensity increasing from the ends of the cross to its center. Outside the heterogeneity, we, as expected, see no fluid motion. As with the results for fractured media, this result qualitatively agrees with the previous studies using Biot theory [2]. However, the porosity in our case is closer to limit cases, which can be a problem for Biot equations applicability. Moreover, reliable results obtained for the considered porosity value show a future transition to a pure single-phase case possible in the study. This advantage is useful for modeling the single pore and fluid behavior within it, including so-called "squirt flow" processes within it.

6 Conclusion

In our work, we presented an approach to numerical modeling of the loading of samples of heterogeneous poroelastic fluid-saturated material based on the theory of thermodynamically compatible systems. In particular, we applied

a quasi-static approximation of the propagation equations for small-amplitude waves, excluding phase acceleration from the system. By expressing stresses in terms of displacements, we obtained a system of second-order partial differential equations for mixture displacements and relative phase displacements. Closing the system by the boundary conditions, we defined the boundary value problem of sample loading. To solve the problem numerically, a second-order finite-difference scheme on a staggered grid is applied using the averaging of material parameters at the boundaries of inhomogeneities and the immersed boundary method to approximate the boundary conditions for stresses and fluid velocity. The resulting SLAE is then solved numerically by specifying the displacement fields inside the computational domain. The presented approach was tested on the problem of uniaxial loading of a fractured sample to monitor the emerging fluid flows inside the cracks. The results show the presence of both crack-to-background and crack-to-crack fluid flow at different typical frequencies, and the demonstrated fluid displacement behavior depends on the frequency of the loading process. This behavior is qualitatively similar to the results based on the well-known Biot theory of poroelasticity. Quantitative analysis of the solution by comparing our algorithm with other two-phase media approaches will be the topic to continue our study. Note that our results were obtained under the simplified assumption of an infinite shear stress relaxation time $\tau \to \infty$, so the case of finite τ will be considered in the future. Moreover, there are computational limitations when using a direct solver, and in order to apply our approach to larger computational domains, we should explore the use of other SLAE solvers, in particular, iterative ones, to obtain the SLAE solution, which is also in our future research plans.

References

1. Rubino, J.G., Muller, T.M., Guarracino, L., Milani, M., Holliger, K.: Seismoacoustic signatures of fracture connectivity. J. Geophys. Res. Solid Earth **119**(3), 2252–2271 (2014)
2. Quintal, B., Rubino, J.G., Caspari, E., Holliger, K.: A simple hydromechanical approach for simulating squirt-type flow. Geophysics **81**(4), D335–D344 (2016)
3. Godunov, S., Romenskii, E.: Elements of Continuum Mechanics and Conservation Laws. Kluwer Academic/Plenum Publishers, New York (2003)
4. Peshkov, I., Pavelka, M., Romenski, E., Grmela, M.: Continuum mechanics and thermodynamics in the Hamilton and the Godunov-type formulations. Continuum Mech. Thermodyn. **30**, 1343–1378 (2018)
5. Romenski, E., Reshetova, G., Peshkov, I., Dumbser, M.: Modeling wavefields in saturated elastic porous media based on thermodynamically compatible system theory for two-phase solid-fluid mixtures. Comput. Fluids **206**, 104587 (2020)
6. Reshetova, G., Romenski, E.: Diffuse interface approach to modeling wavefields in a saturated porous medium. Appl. Math. Comput. **398**, 125978 (2021)
7. Romenski, E., Reshetova, G., Peshkov, I.: Computational model for compressible two-phase flow in deformed porous medium. In: Gervasi, O., et al. (eds.) ICCSA 2021. LNCS, vol. 12949, pp. 224–236. Springer, Cham (2021). https://doi.org/10.1007/978-3-030-86653-2_16

8. Romenski, E., Reshetova, G., Peshkov, I.: Two-phase hyperbolic model for porous media saturated with a viscous fluid and its application to wavefields simulation. Appl. Math. Model. **106**, 567–600 (2022)
9. Novikov, M.A., Lisitsa, V.V., Bazaikin, Y.V.: Wave propagation in fractured-porous media with different percolation length of fracture systems. Lobachevskii J. Math. **41**(8), 1533–1544 (2020)
10. Samarskii, A.A.: The Theory of Difference Schemes, Pure and Applied Mathematics, vol. 240. CRC Press, Boca Raton (2001)
11. Mittal, R., Iaccarino, G.: Immersed boundary methods. Annu. Rev. Fluid Mech. **37**(1), 239–261 (2005)
12. Quintal, B., Steeb, H., Frehner, M., Schmalholz, S.M.: Quasi-static finite-element modeling of seismic attenuation and dispersion due to wave-induced fluid flow in poroelastic media. J. Geophys. Res. **116**, B01201 (2011)
13. Rubino, J.G., Caspari, E., Müller, T.M., Milani, M., Barbosa, N.D., Holliger, K.: Numerical upscaling in 2-D heterogeneous poroelastic rocks: anisotropic attenuation and dispersion of seismic waves. J. Geophys. Res. Solid Earth **121**(9), 6698–6721 (2016)
14. Caspari, E., et al.: Attenuation mechanisms in fractured fluid-saturated porous rocks: a numerical modelling study. Geophys. Prospect. **67**(4), 935–955 (2019)
15. Solovyev, S., Novikov, M., Lisitsa, V.: A numerical investigation of wave-induced fluid flows in anisotropic fractured porous media. Comput. Math. Appl. **140**, 78–88 (2023)
16. Lissa, S., Ruf, M., Steeb, H., Quintal, B.: Digital rock physics applied to squirt flow. Geophysics **86**(4), MR235–MR245 (2021)
17. Alkhimenkov, Y., Quintal, B.: An accurate analytical model for squirt flow in anisotropic porous rocks — Part 2: complex geometry. Geophysics **87**(6), MR291–MR302 (2022)